Convergence of the solutions of the 2D-1V ion drift kinetic equation with wall boundary conditions: manufactured solutions tests

M. R. Hardman[1,2], J. Omotani[3], M. Barnes[2], S. L. Newton[3], and F. I. Parra[4]

[1] Tokamak Energy Ltd, 173 Brook Drive, Milton Park, Abingdon, OX14 4SD, United Kingdom
[2] Rudolf Peierls Centre for Theoretical Physics, University of Oxford, Clarendon Laboratory, Parks Road, Oxford OX1 3PU, United Kingdom
[3] Culham Centre for Fusion Energy, Culham Science Centre, Abingdon, Oxon, OX14 3DB, United Kingdom
[4] Princeton Plasma Physics Laboratory, P.O. Box 451, Princeton, New Jersey 08540, United States

E-mail: michael.hardman@tokamakenergy.co.uk

1. Introduction

The aim of this report is to describe an investigation into the convergence of 2D edge plasma model with collisionless kinetic ions and wall boundary conditions. Previous reports introduced tests using the method of manufactured solutions – these tests highlighted poor convergence of the numerical implementation of the 'moment kinetics' model in the presence of wall boundaries in two spatial dimensions. In this document, we will demonstrate the causes of the observed poor convergence. One source of poor convergence is due to the interaction between the choice of numerical scheme and the form of the ion wall boundary condition. We show that this issue can be adequately resolved by a judicious choice of numerical resolutions in the simulations that we have carried out. The second source of convergence issues is due to a wave-like instability that emerges in simulations with a radial coordinate and a temperature gradient in the coordinate that measures distance to the wall plate. This instability can be suppressed with adequate numerical dissipation in the model.

The report is structured as follows. First, in the next section, we introduce the non-dimensionalised form of the model which we solved numerically. In section 3, we introduce a manufactured solution test appropriate for testing the evolution of the charged particle distribution function. In section 4, we show the results of this test into contrasting cases: first, when there is no radial electric field and we find good convergence, and second when a constant-in-time-and-space radial electric field is imposed, causing poor convergence with increasing resolution. In section 5, we propose an optimisation to address these numerical difficulties in 1D. In section 6 we discuss

whether or not this solution might be generalised to the full 2D model. In section 7 we carry out a manufactured solution test in the 2D model that is designed to avoid the convergence issues highlighted in the rest of this report. We find that the simulation is dominated by an instability that may be of numerical or physical origin. Radial numerical diffusion is used to suppress the instability and demonstrate convergence. In section 8, we utilise the radial numerical diffusion to demonstrate that the numerical implementation converges in a 2D manufactured solution test which has a nonzero radial electric field at the wall boundaries. This result demonstrates that the model is correctly implemented using the chosen methods. In section 9, we test the convergence of physical solutions to the model equations where the source of ions is due to a constant, uniform ionisation of neutral particles. Finally, in section 10, we discuss our results.

The input files for the tests presented in this report are named in Appendix A (grouped by figure) and found in supporting documentation.

2. The model ion drift kinetic equations

The system that we consider consists of a single ion species of charge e and mass m_i, and an electron species that is modelled as having a Boltzmann response. The magnetic field is taken to be helical, with the form

$$\mathbf{B} = B_z \hat{\mathbf{z}} + B_\zeta \hat{\boldsymbol{\zeta}}, \tag{1}$$

where (r, z, ζ) are cylindrical coordinates, and B_z and B_ζ are constant in z, r, and ζ. See figure 1. The coordinate ζ is the analogue of the toroidal angle in a more realistic tokamak open-field line geometry, and z is the analogue of the vertical coordinate. We take the ions to be collisionless for simplicity. We apply wall boundary conditions in z. In sections 4-6 we solve a 1D model that does not include a radial domain. In section 7, we solve the model with a radial domain and we impose periodic boundary conditions in r. We assume that the plasma equilibrium is independent of ζ.

In Table 1, we define normalised and reference quantities. Consistent with previous reports, normalised variables are denoted with a tilde. In terms of the normalised variables, the model system of equations takes the following form. The collisionless drift-kinetic equation for ions is

$$\frac{\partial \widetilde{F}_i}{\partial \tilde{t}} + \left(b_z \tilde{v}_\parallel - \frac{\rho_*}{2} \widetilde{E}_r \right) \frac{\partial \widetilde{F}_i}{\partial \tilde{z}} + \frac{\rho_*}{2} \widetilde{E}_z \frac{\partial \widetilde{F}_i}{\partial \tilde{r}} + \frac{b_z \widetilde{E}_z}{2} \frac{\partial \widetilde{F}_i}{\partial \tilde{v}_\parallel} = \widetilde{S}_i + \nu_r \frac{\partial^2 \widetilde{F}_i}{\partial \tilde{r}^2} + \nu_v \frac{\partial^2 \widetilde{F}_i}{\partial \tilde{v}_\parallel^2}, \tag{2}$$

where and ν_r and ν_v are numerical viscosity coefficients, and $\rho_* = c_{\text{ref}}/L_{\text{ref}}\Omega_{\text{ref}}$ is a small parameter that measures the size of the ion gyro-orbits compared to the macroscopic size of the system. Note that b_z is also a small parameter in the formal ordering of the 2D model [1, 2]. The quasineutrality condition takes the form

$$\widetilde{n}_i = \widetilde{n}_e = \widetilde{N}_e \exp\left(\frac{\widetilde{\phi}}{\widetilde{T}_e} \right), \tag{3}$$

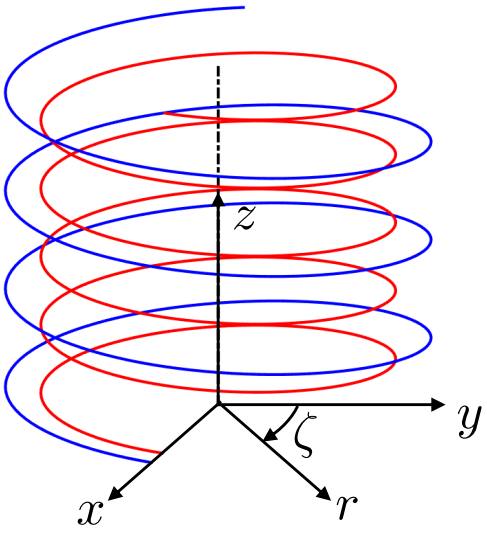

Figure 1: The form of the magnetic field and the left-handed coordinates (r, z, ζ) in terms of the right-handed cartesian (x, y, z). Taken from [1].

and is used to determine the potential $\widetilde{\phi}$. The normalised electric fields are derived from the potential, and are defined by

$$\widetilde{E}_z = -\frac{\partial \widetilde{\phi}}{\partial \tilde{z}}, \text{ and } \quad \widetilde{E}_r = -\frac{\partial \widetilde{\phi}}{\partial \tilde{r}}. \tag{4}$$

and the ion density is defined by

$$\widetilde{n}_i = \frac{1}{\sqrt{\pi}} \int_{-\infty}^{\infty} d\tilde{v}_{\parallel} \int_{0}^{\infty} 2d\tilde{v}_{\perp} \tilde{v}_{\perp} \widetilde{F}_i. \tag{5}$$

The boundary condition on the ion distribution function is that no particles return from the wall, i.e.,

$$\begin{aligned} \widetilde{F}_i(\tilde{z} = -\tilde{L}_z/2, \tilde{v}_{\parallel} > \rho_* \widetilde{E}_r/2b_z, \tilde{v}_{\perp}, \tilde{t}) &= 0 \\ \widetilde{F}_i(\tilde{z} = \tilde{L}_z/2, \tilde{v}_{\parallel} < \rho_* \widetilde{E}_r/2b_z, \tilde{v}_{\perp}, \tilde{t}) &= 0, \end{aligned} \tag{6}$$

where $\tilde{L}_z = L_z/L_{\text{ref}}$. Note that this boundary condition implies that a source of ions is required for a nontrivial steady-state solution. Since we wish to avoid the complication of including a neutral species for the purposes of this report, we achieve a steady-state solution by imposing appropriate sources $\widetilde{S}_i$. The remainder of this report is an investigation into how the boundary condition (6) interacts with the spectral-element numerical method chosen to implement these equations. It is useful to think in terms of the total ion velocity in the $\tilde{z}$ direction

$$\tilde{v}_z(\tilde{v}_{\parallel}, \tilde{z}, \tilde{r}) = b_z \tilde{v}_{\parallel} - \frac{\rho_*}{2} \widetilde{E}_r(\tilde{z}, \tilde{r}), \tag{7}$$

norm. variable	definition
$\tilde{t}$	$t(c_{\rm ref}/L_{\rm ref})$
$\tilde{z}$	$z/L_{\rm ref}$
$\tilde{r}$	$r/L_{\rm ref}$
$\tilde{v}_\parallel$	$v_\parallel/c_{\rm ref}$
$\tilde{v}_\perp$	$v_\perp/c_{\rm ref}$
$\tilde{v}_z$	$v_z/c_{\rm ref}$
$\tilde{v}_r$	$v_r/c_{\rm ref}$
$\tilde{v}_\zeta$	$v_\zeta/c_{\rm ref}$
$\widetilde{N}_e$	$N_e/n_{\rm ref}$
$\tilde{n}_s$	$n_s/n_{\rm ref}$
$\widetilde{\phi}$	$e\phi/T_{\rm ref}$
$\widetilde{E}_r$	$eL_{\rm ref}E_r/T_{\rm ref}$
$\widetilde{E}_z$	$eL_{\rm ref}E_z/T_{\rm ref}$
$\tilde{R}_{\rm in}$	$R_{\rm in}(n_{\rm ref}L_{\rm ref}/c_{\rm ref})$
$\tilde{R}_{\rm ion}$	$R_{\rm ion}(n_{\rm ref}L_{\rm ref}/c_{\rm ref})$
$\widetilde{F}_s$	$F_s(c_{\rm ref}^3\pi^{3/2}/n_{\rm ref})$
$\widetilde{S}_s$	$S_s(c_{\rm ref}^3\pi^{3/2}L_{\rm ref}/n_{\rm ref}c_{\rm ref})$
ρ_*	$c_{\rm ref}/L_{\rm ref}\Omega_{\rm ref}$
b_z	B_z/B

ref. quantity	definition
$L_{\rm ref}$	ref. length (m)
$T_{\rm ref}$	ref. temperature (KeV)
$n_{\rm ref}$	ref. density ($\rm m^{-3}$)
$c_{\rm ref}$	$\sqrt{2T_{\rm ref}/m_i}$ ($\rm ms^{-1}$)
m_i	ion mass (kg)
$B_{\rm ref}$	ref. B (T)
$\Omega_{\rm ref}$	$eB_{\rm ref}/m_i$ ($\rm s^{-1}$)

Table 1: Definitions for normalised and reference quantities used in the report.

where we have indicated that $\tilde{v}_z$ is a function of $(\tilde{v}_\parallel, \tilde{z}, \tilde{r})$ because $\widetilde{E}_r$ is a function of position. Note that in general, if the magnetic field $\mathbf{B}$ varies with position, then $(\tilde{z}, \tilde{r})$ dependence will also arise from the geometrical coefficients appearing in equation (7). It is important to note that as a consequence of this dependence on position, the boundary condition (6) must be applied on a potentially non-trivial $(\tilde{v}_\parallel, \tilde{r})$ contour in phase space. This detail will be important in the following discussion.

The model described above solves for $\widetilde{F}_i = \widetilde{F}_i(\tilde{v}_\parallel, \tilde{v}_\perp, \tilde{z}, \tilde{r})$. The coordinate $\tilde{v}_\perp$ is a conserved quantity because of the assumption of a spatially homogeneous magnetic field strength B. In addition, $\tilde{v}_\perp$ does not appear anywhere explicitly in the coefficients of the drift kinetic equation. This is a result of the fact that we have neglected the neutral species. We can reduce the complexity and computational time of our simulations by marginalising over the $\tilde{v}_\perp$ coordinate by solving for the distribution

$$\widetilde{f}_i(\tilde{v}_\parallel, \tilde{z}, \tilde{r}) = \int_0^\infty 2d\tilde{v}_\perp \tilde{v}_\perp \widetilde{F}_i(\tilde{v}_\parallel, \tilde{v}_\perp, \tilde{z}, \tilde{r}). \tag{8}$$

We make use of this reduction in the remainder of this report by choosing the initial $\widetilde{F}_i(\tilde{v}_\parallel, \tilde{v}_\perp, \tilde{z}, \tilde{r})$ such that

$$\widetilde{F}_i(\tilde{v}_\parallel, \tilde{v}_\perp = 0, \tilde{z}, \tilde{r}) = \int_0^\infty 2d\tilde{v}_\perp \tilde{v}_\perp \widetilde{F}_i(\tilde{v}_\parallel, \tilde{v}_\perp, \tilde{z}, \tilde{r}), \tag{9}$$

and evolving $\widetilde{F}_i(\tilde{v}_\parallel, \tilde{v}_\perp = 0, \tilde{z}, \tilde{r})$.

3. Testing the numerical implementation with the method of manufactured solutions

To test the numerical implementation of the system described above, we prescribe a manufactured solution that satisfies the ion boundary conditions, and then proceed to compute symbolically the appropriate $\widetilde{S}_i$ that would maintain this solution. Then, we use this symbolically computed $\widetilde{S}_i$ in our numerical implementation, and confirm that the numerical solution remains close to the prescribed symbolic solution. For maximum simplicity, we carry out only steady-state tests with no explicit time dependence in the manufactured solutions.

In what follows, we perform a numerical simulations for a fixed time $\tilde{t} = 1$ for varying resolutions. We check that the numerical solution is consistent with the target manufactured solution by confirming that the numerical error reduces towards zero as the resolution increases. To measure the error between the numerical solution and the target manufactured solution, we introduce the following measures. We define an error on the ion density

$$\epsilon(\widetilde{n}_i) = \sqrt{\frac{\sum_{i,j} |\widetilde{n}_i(z_i, r_j) - \widetilde{n}_i^{MS}(z_i, r_j)|^2}{N_r N_z}}, \tag{10}$$

where $\widetilde{n}_i^{MS}$ is the target manufactured density, and N_r and N_z are the total number of points in the r and z grids, respectively. We define similar errors on the $\widetilde{\phi}$ and $\widetilde{E}_z$, these are

$$\epsilon(\widetilde{\phi}) = \sqrt{\frac{\sum_{i,j} |\widetilde{\phi}(z_i, r_j) - \widetilde{\phi}^{MS}(z_i, r_j)|^2}{N_r N_z}}, \tag{11}$$

and

$$\epsilon(\widetilde{E}_z) = \sqrt{\frac{\sum_{i,j} |\widetilde{E}_z(z_i, r_j) - \widetilde{E}_z^{MS}(z_i, r_j)|^2}{N_r N_z}}, \tag{12}$$

respectively. We define an error on the ion distribution function

$$\epsilon(\widetilde{F}_i) = \sqrt{\frac{\sum_{i,j,k,l} |\widetilde{F}_i(v_{\parallel i}, v_{\perp j}, z_k, r_l) - \widetilde{F}_i^{MS}(v_{\parallel i}, v_{\perp j}, z_k, r_l)|^2}{N_{v_\parallel} N_{v_\perp} N_r N_z}}, \tag{13}$$

where $N_{v_\parallel}$ and $N_{v_\perp}$ are the total number of points in the $v_\parallel$ and $v_\perp$ grids, respectively. The errors $\epsilon(\widetilde{n}_s)$, $\epsilon(\widetilde{F}_i)$, and $\epsilon(\widetilde{F}_n)$ measure the average error per point in the array of the numerical solution.

As noted previously [3], `Julia` has support for elements of symbolic algebra via the `Symbolics.jl` package [4, 5]. This allows us to partially automate the process of calculating the manufactured sources. Currently, the `Symbolics.jl` package supports symbolic differentiation, allowing for a great reduction in the effort of developing manufactured solutions tests. Unfortunately, symbolic integration is not yet supported by the `Symbolics.jl` package, so the target manufactured solutions must be chosen to be sufficiently simple to integrate by hand.

We must construct a manufactured ion distribution function that satisfies the necessary boundary conditions. We can achieve this by constructing a distribution function from the velocity coordinate $\overline{v}_\parallel = \tilde{v}_\parallel - \alpha\rho_* \widetilde{E}_r/2b_z$, where α takes the values of 0 or 1 depending on the type of test carried out. We choose

$$\widetilde{F}_i = \left[H\left(\overline{v}_\parallel\right) \overline{v}_\parallel^p \left(\frac{1}{2} + \frac{\tilde{z}}{\tilde{L}_z}\right) n_+(\tilde{z},\tilde{r}) + H\left(-\overline{v}_\parallel\right) \overline{v}_\parallel^p \left(\frac{1}{2} - \frac{\tilde{z}}{\tilde{L}_z}\right) n_-(\tilde{z},\tilde{r}) + \left(\frac{1}{2} - \frac{\tilde{z}}{\tilde{L}_z}\right)\left(\frac{1}{2} + \frac{\tilde{z}}{\tilde{L}_z}\right) n_0(\tilde{z},\tilde{r}) \right] \exp\left(-\overline{v}_\parallel^2 - \tilde{v}_\perp^2\right), \tag{14}$$

with p a power chosen to be either $p = 2$ or 4, and $H\left(x\right)$ the Heaviside function, taking the values 1 for $x > 0$ and 0 for $x < 0$. In the `Julia` implementation $H\left(0\right) = 1/2$. Note that the forward going part of the distribution vanishes at $\tilde{z} = -L_z/2$ and the backward going part vanishes at $\tilde{z} = L_z/2$ – ensuring that condition (6) holds. The velocity space dependence is chosen so that $\partial\widetilde{F}_i/\partial\tilde{v}_\parallel = 0$ at $\tilde{v}_z(\tilde{v}_\parallel, \tilde{z} = \pm L_z/2, \tilde{r}) = 0$. This also has the effect that this manufactured solution marginally satisfies the Chodura condition [6] for $\alpha = 0$ and $p = 2$, and oversatisfies the Chodura condition for $\alpha = 0$ and $p = 4$. See appendix Appendix B for a further discussion. The option of using $p = 4$ has been introduced to permit the later addition of a $\tilde{v}_\parallel$ diffusion operator into the drift kinetic equation. For $p = 2$, the manufactured solution is only continuous at $\tilde{v}_\parallel = 0$ up to and including the first derivative in $\tilde{v}_\parallel$, whereas for $p = 4$ the manufactured solution is continuous at $\tilde{v}_\parallel$ up to and including the third derivative in $\tilde{v}_\parallel$. In principle, we could specify any functions for $n_+(\tilde{z},\tilde{r})$, $n_-(\tilde{z},\tilde{r})$ and $n_0(\tilde{z},\tilde{r})$ that satisfy the radial boundary conditions.

To specify the ion density, needed to compute the potential via quasineutrality, we compute the velocity integral of equation (14) analytically. The result is

$$\widetilde{n}_i = a n_+(\tilde{z},\tilde{r}) \left(\frac{1}{2} + \frac{\tilde{z}}{\tilde{L}_z}\right) + a n_-(\tilde{z},\tilde{r}) \left(\frac{1}{2} - \frac{\tilde{z}}{\tilde{L}_z}\right) + n_0(\tilde{z},\tilde{r}) \left(\frac{1}{2} + \frac{\tilde{z}}{\tilde{L}_z}\right)\left(\frac{1}{2} - \frac{\tilde{z}}{\tilde{L}_z}\right), \tag{15}$$

where $a = 1/4$ if $p = 2$ and $a = 3/8$ if $p = 4$. Finally, we specify forms for $n_\pm$ and n_0 that allow us to study cases with periodic boundary conditions in $\tilde{r}$. These are

$$n_\pm = \exp\left[\left(\epsilon + \frac{1}{2} \mp \frac{\tilde{z}}{\tilde{L}_z}\right)^{1/2}\right] n_0, \tag{16}$$

and

$$n_0 = \exp\left[1 + \frac{1}{20}\sin\left(\frac{2\pi\tilde{r}}{\tilde{L}_r}\right)\left((1-\alpha)\cos\left(\frac{\pi\tilde{z}}{\tilde{L}_z}\right) + \alpha\right)\right], \tag{17}$$

with $\tilde{L}_r = L_r/L_{\text{ref}}$.

4. Tests in 1D: neglecting the radial dimension

The simplest test of the model is to examine the case where we assume that the plasma is homogeneous in the radial direction. Then, $\widetilde{E}_r = 0$ and $\overline{v}_\parallel = \tilde{v}_\parallel$. For this test, we take $\tilde{r} = 0$ and hence

$$n_\pm = \exp\left[1 + \left(\epsilon + \frac{1}{2} \mp \frac{\tilde{z}}{\tilde{L}_z}\right)^{1/2}\right], \tag{18}$$

with $\epsilon = 0.1$, and

$$n_0 = \exp[1]. \tag{19}$$

These functions are chosen so that $\widetilde{E}_z = O\left(\left(\epsilon + 1/2 \mp \tilde{z}/\tilde{L}_z\right)^{-1/2}\right)$ as $\tilde{z} \to \pm\tilde{L}_z/2$ – this is inspired by the properties of collisional sheaths [7] and magnetic presheaths [6]. The parameter ϵ is required to prevent $\widetilde{E}_z$ diverging to infinity within the numerical simulation domain. We take $\nu_r = \nu_v = 0$ for simplicity. In figure 2, we show the result of carrying out this test for $N_{grid} = 17$ points per element and equal number of elements in each coordinate dimension. We take the time step to be $\Delta\tilde{t} = 0.004/N_{element}$. We note the excellent convergence shown in figure 2: the scaling of the numerical errors is linear on a log-log plot, consistent with spectral accuracy.

The high-order spectral convergence seen in figure 2 is extremely sensitive to the location in $\tilde{v}_\parallel$ where the boundary condition (14) is imposed. Recall that this location is determined by the algebraic equation $\tilde{v}_z(\tilde{v}_\parallel, \tilde{r}) = 0$, where $\tilde{v}_z$ is defined in equation (7). We can see how a nonzero radial electric field interacts with the boundary condition (14) by imposing a constant $\widetilde{E}_r = 0.5$ in the manufactured solution test described above. We take $\alpha = 1$ so that the manufactured solution satisfies the ion wall boundary condition. The results of this test are shown in figure 3. Note that we keep the same resolution parameters as the test described in figure 2, and we keep the same formulae for $n_\pm$, and n_0. Despite using the same numerical resolutions, figure 3 shows much larger numerical errors than figure 2. We can see that the errors are reducing slowly with increasing numerical resolution, but the trends of the errors are troubling, potentially indicating that the errors will not reach machine precision levels even with very large resolution. The errors in $\widetilde{E}_z$ are much larger than in the other fields, suggesting that any physics simulation with a nonzero $\widetilde{E}_r$ would suffer severe numerical difficulties. This is consistent with behaviour reported previously when a radial domain and nonzero $\widetilde{E}_r$ were included.

We can improve on the trend of the convergence shown in figure 3 by using low-order elements. In figure 4 we show the results of the MMS test where we have used $N_{grid} = 5$ in the $\tilde{v}_\parallel$ and $\tilde{z}$ dimensions, and increased the number of elements to match the number of points as in the cases in figure 3 for a fair comparison. We see that

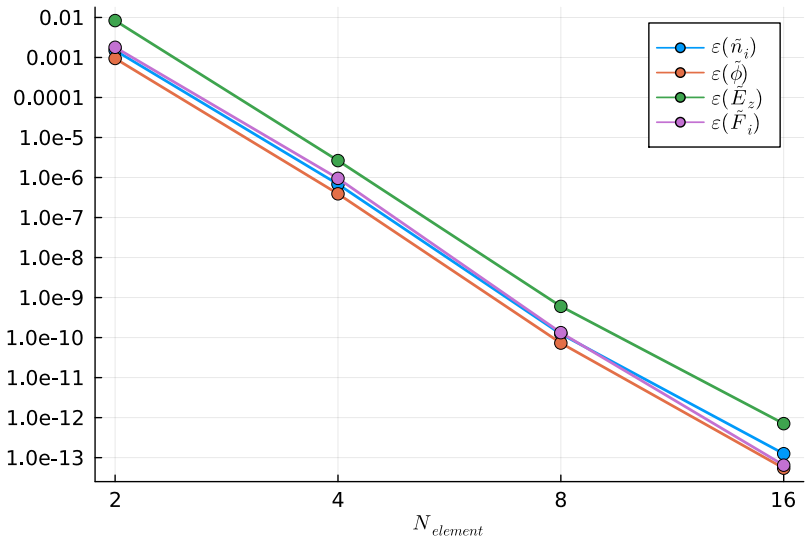

Figure 2: Manufactured solution test using the prescribed solution (14) as an initial condition with consistent source S_i computed analytically from equation (2). We take $\widetilde{E}_r = 0$ and neglect the radial dimension by taking $n_\pm$ and n_0 as in equations (18) and (19). We take $\rho_* = b_z = \widetilde{T}_e = \widetilde{N}_e = 1.0$. Each element has $N_{grid} = 17$ points in and we take the $\tilde{v}_\parallel$ and $\tilde{z}$ dimensions to have an equal number of elements $N_{element}$. We take the maximum $\tilde{v}_\parallel = 6$. We run for $250 \times N_{element}$ steps with $\Delta\tilde{t} = 0.004/N_{element}$ so that the final $\tilde{t} = 1$.

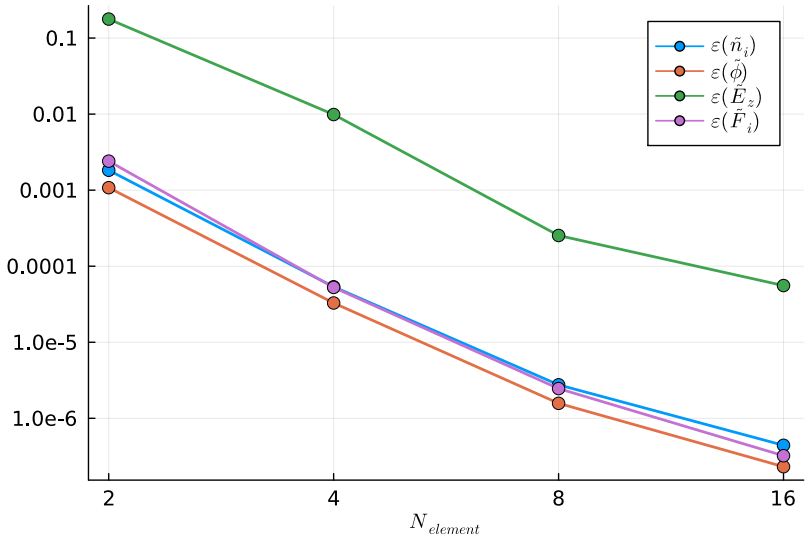

Figure 3: The same test a presented in figure 2 but with $\widetilde{E}_r = 0.5$. We continue to neglect other aspects of the radial dimension – only a constant $\widetilde{E}_r$ is imposed. This is equivalent to shifting the $\tilde{v}_\parallel$ grid by an amount $\rho_*\widetilde{E}_r/2b_z$. Note that the spectral convergence of the code is destroyed by this shift, with particularly troubling errors in $\widetilde{E}_z$, and no clear linear trend on the log-log scale.

using low-order elements allows us to recover an almost linear scaling for the errors on the log-log scale, although the absolute values of the errors are not improved for the resolutions used here. It is expected that a low-order method should require more points to reach the same level of residual errors. A further improvement can clearly be

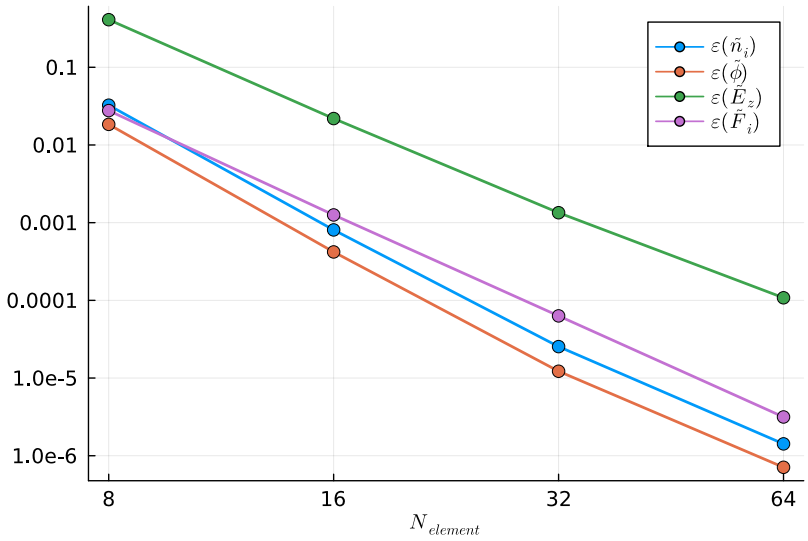

Figure 4: The same test a presented in figure 3 but with $N_{grid} = 5$ instead of $N_{grid} = 17$. Using these low-order elements, we recover an almost linear scaling of the errors, suggesting that with adequate resolution, the nonspectral behaviour due to the wall boundary condition can be avoided.

obtained by simply using higher resolution in the low-order scheme. We find that it is most important to use high $\tilde{v}_{\|}$ resolution. In figure 5 we show the result of increasing the number of $\tilde{v}_{\|}$ elements by a factor of 4 compared to the number of $\tilde{z}$ elements, at fixed $N_{grid} = 5$. The errors are reduced by almost two orders of magnitude. We adopt this partition between spatial and velocity resolution when we simulate 2D cases.

5. Resolution of the inaccurate behaviour of spectral methods on nonpolynomial functions

We can understand the behaviour seen in the 1D-1V manufactured solutions test if we consider a simple test case. Noting that the manufactured solution involves the Heaviside function $H(x)$, we anticipate that numerical differentiation of the manufactured solution is likely to introduce numerical artifacts into the solution. This is not entirely artificial, as the real solution must obey the boundary condition (14), and so the real solution will have a discontinuity in a higher order derivative when a spectral representation is used. With this in mind, we consider the function

$$f(x) = H(x)\, x^2, \tag{20}$$

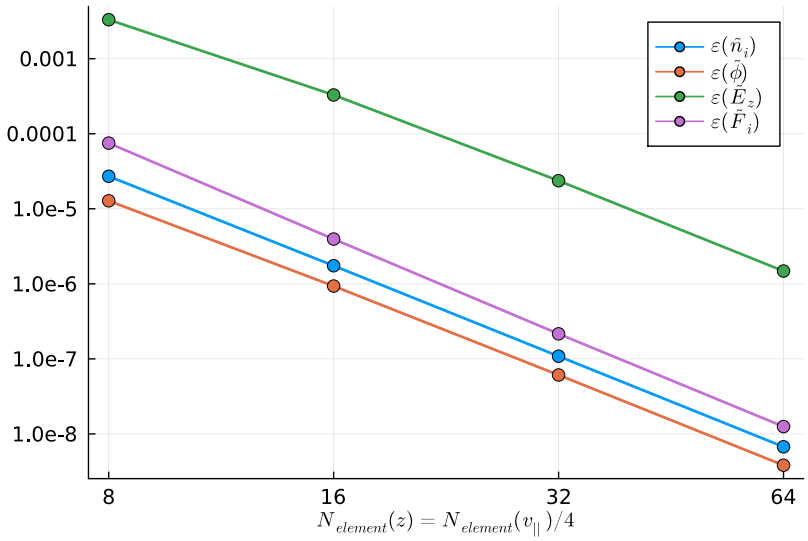

Figure 5: The same test a presented in figure 3 but with $N_{grid} = 5$ instead of $N_{grid} = 17$ and $N_{element}(\tilde{z}) = N_{element}(\tilde{v}_{||})/4$.

represented on the Chebyshev polynomial colocation grid in a single element. We then compare the numerical result of differentiating this function using the Chebyshev transforms to the exact result

$$\frac{\mathrm{d}f}{\mathrm{d}x} = \begin{cases} 0 & x < 0 \\ 2x & x \geq 0 \end{cases} . \tag{21}$$

This comparison is given in figure 6 using $N_{grid} = 9$ points in the Chebyshev grid. We note that whilst the first derivative is continuous at the origin $x = 0$, the second derivative of the function $f(x)$ is discontinuous at $x = 0$. The result is that the differentiation using the spectral method introduces Gibbs phenomena everywhere within the element. This phenomenon can be avoided if we take care to take the derivative with information from the region of the function where $f(x) > 0$. This could be achieved by using a cubic spline within the element to fit the function in the appropriate region of x and then take the derivative to be that given by the cubic spline fit. This is illustrated in figure 7, where the `Dierckx` package is used to compute a derivative using only data from within the spline fit domain.

6. Complications arising in the 2D case

In the previous section, we proposed a solution to the problem of taking a derivative of a function that has the form given by equation (20). Although we have not implemented this solution in 'moment kinetics', this optimisation could increase the accuracy of derivatives within the elements where a boundary condition is applied on internal points. In this section we demonstrate that there is a more subtle problem in generalising this solution to the 2D case where we must include a radial dimension $\tilde{r}$. Consider figure

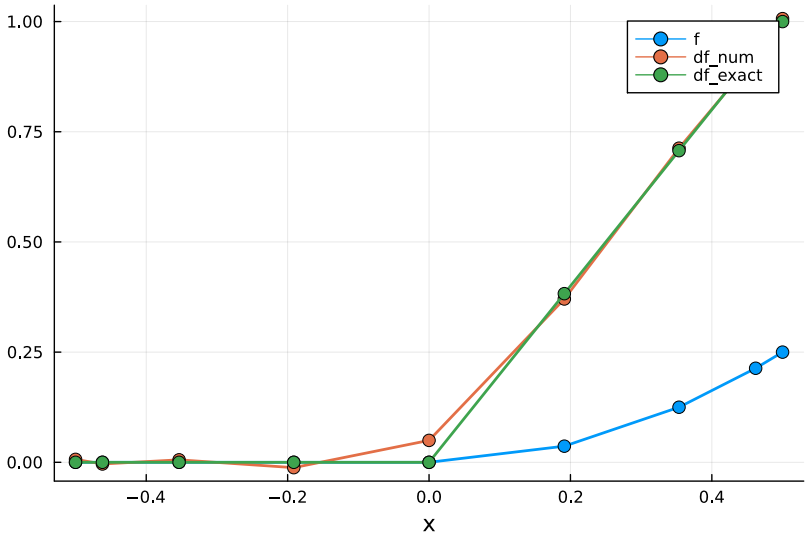

Figure 6: Simple test using the spectral method to calculate $\mathrm{d}f/\mathrm{d}x$ (`df_num`) with a comparison to the exact derivative (`df_exact`). Note the presence of Gibbs ringing because the element boundary does not coincide with where $f(x) = 0$.

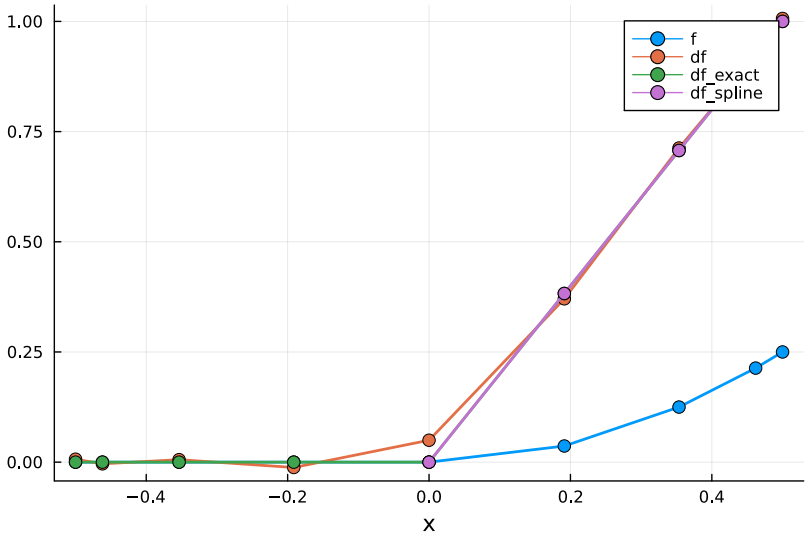

Figure 7: Simple test using the spectral method to calculate $\mathrm{d}f/\mathrm{d}x$ (`df_num`) with a comparison to the exact derivative (`df_exact`) and a derivative taken using a cubic spline over the positive data (`df_spline`).

8. The figure shows the phase space of the distribution function F_i at the wall plates $\tilde{z} = \pm\tilde{L}_z/2$. We note that the radial electric field $\widetilde{E}_r(\tilde{z}, \tilde{r})$ will have a different functional form at each of the wall plates, and that the sign of the $\tilde{v}_\parallel$ axis depends on whether one inspects the upper or lower wall plate in $\tilde{z}$. In the 1D problem previously considered in this report, we have attempted to address the situation where the contour of $\tilde{v}_z(\tilde{v}_\parallel, \tilde{r}) = 0$ is a straight line in the $(\tilde{v}_\parallel, \tilde{r})$ plane, parallel to the $\tilde{r}$ axis crossing $\tilde{r} = 0$ at a fixed value of $\tilde{v}_\parallel \neq 0$. In the 2D case the $\tilde{v}_z(\tilde{v}_\parallel, \tilde{r}) = 0$ contour may take a nontrivial form, meaning that we must take care when taking $\tilde{r}$ derivatives of $\widetilde{F}_i$. This is because we have observed that it is important to avoid taking a derivative on $\widetilde{F}_i$ data that is enforced to be zero by the boundary condition, and a radial derivative in the region of $\tilde{v}_\parallel$ near the boundary will necessarily do this using the default spectral element method.

The resolution of this problem is not obvious. One possible solution would be to use the cubic spline method proposed in the last section for both the $\tilde{r}$ and $\tilde{v}_\parallel$ coordinates separately. However, care would be required to make sure that multiple crossings of the $\tilde{v}_z(\tilde{v}_\parallel, \tilde{r}) = 0$ contour did not occur in each $\tilde{r}$ element. This may be difficult to ensure in a turbulent problem when oscillations in $\widetilde{E}_r$ in $\tilde{r}$ should be expected. Another solution could be to change from $\tilde{v}_\parallel$ to $\tilde{v}_z$ coordinates when solving the ion drift kinetic equation. This is also problematic for an explicit code, because changing to these coordinates would require the knowledge of $\partial\widetilde{E}_r/\partial\tilde{t}$ before integrating $\widetilde{F}_i(\tilde{t}^n)$ in time to find $\widetilde{F}_i(\tilde{t}^{n+1})$. A final solution could be to regrid the distribution function $\tilde{v}_\parallel$ elements near the $\tilde{v}_z(\tilde{v}_\parallel, \tilde{r}) = 0$ boundary so that the radial derivatives could be computed by first taking $\partial\widetilde{F}_i/\partial\tilde{r}|_{\tilde{v}_z}$ and then use the chain rule to compute $\partial\widetilde{F}_i/\partial\tilde{r}|_{\tilde{v}_\parallel}$. In light of the fact that $\widetilde{E}_r$ varies with $\tilde{z}$, the regriding must necessarily be local to each of the wall plates. Whether or not this method will improve the convergence in practice is not clear until an implementation is attempted.

Finally, we comment that the convenient assumption of $\partial\widetilde{F}_i/\partial\tilde{v}_\parallel$ on $\tilde{v}_z(\tilde{v}_\parallel, \tilde{r}) = 0$ that was built into the manufactured solution (14) also implies that $\partial\widetilde{F}_i/\partial\tilde{v}_\parallel = 0$ on $\tilde{v}_z(\tilde{v}_\parallel, \tilde{r}) = 0$. This fact means that for solutions of the form of (14) we are able to treat the $\tilde{r}$ and $\tilde{v}_\parallel$ derivatives using the same boundary conditions in the elements including the $\tilde{v}_z(\tilde{v}_\parallel, \tilde{r}) = 0$ contour.

7. Extending the 1D test to 2D whilst avoiding discontinuities off element boundaries

Having developed some intuition for the limitations inherent in the spectral-element scheme, it is interesting to consider a test of the 2D model that avoids the problems associated with having $\widetilde{E}_r \neq 0$ at the wall boundaries. Choosing $\alpha = 0$ and $p = 4$ in the manufactured solution (14) provides such a test. The distribution function is constructed with $H\left(\tilde{v}_\parallel\right)$, meaning that the discontinuities in the $\tilde{v}_\parallel$ derivatives of the function are on element boundaries. With the choice of $\alpha = 0$, using the quasineutrality relation (3) , and the definition (4), one can use equations (15)-(17) to verify that $\widetilde{E}_r = 0$ at $\tilde{z}/\tilde{L}_z = \pm 1/2$. This ensures that the manufactured solution is consistent with the

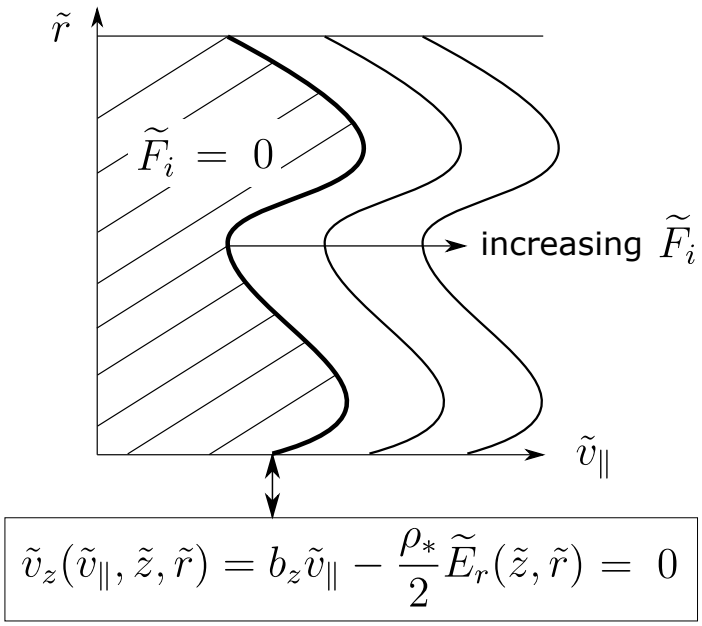

Figure 8: Illustration of the form of the distribution function at $\tilde{z} = \pm L_z/2$, as a consequence of the wall boundary condition (6). The fact that $\widetilde{E}_r = \widetilde{E}_r(\tilde{r})$ at $\tilde{z} = \pm L_z/2$ means that the contour at which $\widetilde{F}_i = 0$ may not be a straight line in the $(\tilde{v}_\parallel, \tilde{r})$ plane. Note that because $\widetilde{E}_r(\tilde{r})$ does not necessarily have the same functional form at $\tilde{z} = \pm L_z/2$, this phase space map will be different at each of $\tilde{z} = \pm L_z/2$.

wall boundary condition (14).

Choosing $\alpha = 0$ and $p = 4$, the manufactured solution (14) has none of the features that caused poor numerical convergence in the 1D test cases with a nonzero $\widetilde{E}_r$. The radial electric field is allowed to be nonzero in the plasma, but it vanishes at the wall, and the distribution function has no discontinuous derivatives except at $v_\parallel$ element boundaries. Therefore, we might expect that numerical simulations of this manufactured solution should show the same convergence properties as in figure 2. However, we find that this manufactured solution is unstable in the absence of numerical diffusion, as we now discuss.

In the 1D case described in figure 2, we were able to obtain good numerical convergence for relatively few elements in the spatial and velocity dimensions. This is not observed in the 2D case. Instead, regardless of the resolution, if $\nu_r = 0$, we typically see an exponential growth in the error with time, coinciding with the growth of oscillatory structures in $\widetilde{E}_r$ and $\widetilde{E}_z$. The simulation eventually crashes when these structures become large enough to force the pressure to be negative.

To illustrate this behaviour with a concrete example, we choose $\nu_r = \nu_v = 0$, $\rho_* = b_z = \widetilde{T}_e = \widetilde{N}_e = 1.0$, $N_{element} = 16$ and $N_{grid} = 5$ for the spatial $(\tilde{z}, \tilde{r})$ dimensions,

and we take $N_{element} = 64$ and $N_{grid} = 5$ for the $\tilde{v}_\parallel$ dimension. These resolution choices are based on the desire to use a lower order method in $(\tilde{z}, \tilde{r}, \tilde{v}_\parallel)$ as discussed in section 4. In figure 9, we show the results of integrating to a time $\tilde{t} = 0.65$ with a timestep size of $\Delta\tilde{t} = 0.001$. We find exponentially growing errors between the numerical and symbolic functions, and a wave-like structure in the $(\tilde{z}, \tilde{r})$ plane. This may indicate the presence of a physical instability to the target solution (15). We note that increasing the $(\tilde{z}, \tilde{r})$ resolutions causes the spatial period of the wave form to get smaller and the growth of the errors to be faster. Typically the wave occurs on a scale comparable to the individual elements. This may be consistent with the fact that drift-kinetic instabilities have no cut-off at high wavenumbers.

A full demonstration of the nature of the instability seen in figure 9c requires a micro-stability calculation around the equilibrium (14). This exercise is left for future work. For now, we carry out the manufactured solutions test for the case with $\alpha = 0$, $p = 4$, taking $N_{grid} = 5$ for the $\tilde{z}$, $\tilde{r}$ and $\tilde{v}_\parallel$ dimensions, scanning in $N_{element}(\tilde{z}) = N_{element}(\tilde{r}) = N_{element}(\tilde{v}_\parallel)/4$ taking $\Delta\tilde{t} = 0.016/N_{element}(\tilde{z})$ and evolving the solution until a time of $\tilde{t} = 1$. We suppress the instability using radial diffusion with $\nu_r = 0.01$, keeping $\nu_v = 0$. The result of this scan is shown in figure 10. We can see that the radial numerical dissipation has allowed us to obtain a performance in this 2D example that is comparable to the performance obtained in 1D in figure 5.

8. The 2D MMS test where $\widetilde{E}_r \neq 0$ at the wall

We are now in a position to turn to the MMS test where we allow $\widetilde{E}_r$ to be non-zero at the wall boundaries. This means that we choose $\alpha = 1$ in the manufactured solution (14). We continue to take $p = 4$ and $\rho_* = b_z = \widetilde{T}_e = \widetilde{N}_e = 1.0$ as in the other tests presented in this report. We use identical numerical resolutions as for the test presented in figure 10, to generate a like-for-like comparison. The result is shown in figure 11, which demonstrates that the numerical implementation of the model is adequate provided that sufficient numerical resolution and low-order elements are used to resolve the physical phenomena of interest. Here, we have applied radial numerical dissipation with $\nu_r = 0.01$ (and $\nu_v = 0.0$) to suppress the instability described in the last section.

It is interesting to plot the ion distribution function $\widetilde{F}_i(\tilde{v}_\parallel, \tilde{r})$ at the wall boundary to connect to the discussion in section 6. Figure 12 shows a sinusoidal structure in the distribution function which corresponds to the form of $\overline{v}_\parallel = \tilde{v}_\parallel - \rho_* \widetilde{E}_r / 2b_z$. The distribution is plotted at $\tilde{t} = 1$ for the highest resolution given in figure 11. It is clear that sufficient resolution must be supplied to adequately resolve the $\overline{v}_\parallel = 0$ contour using the rectangular $(\tilde{v}_\parallel, \tilde{r})$ spectral-element grid. Whether or not the numerical optimisations described in section 6 are ultimately required will be determined by experience using the current numerical implementation in situations where the model includes radial inhomogeneity and Dirichlet boundary conditions. We will explore this question with these features in future work.

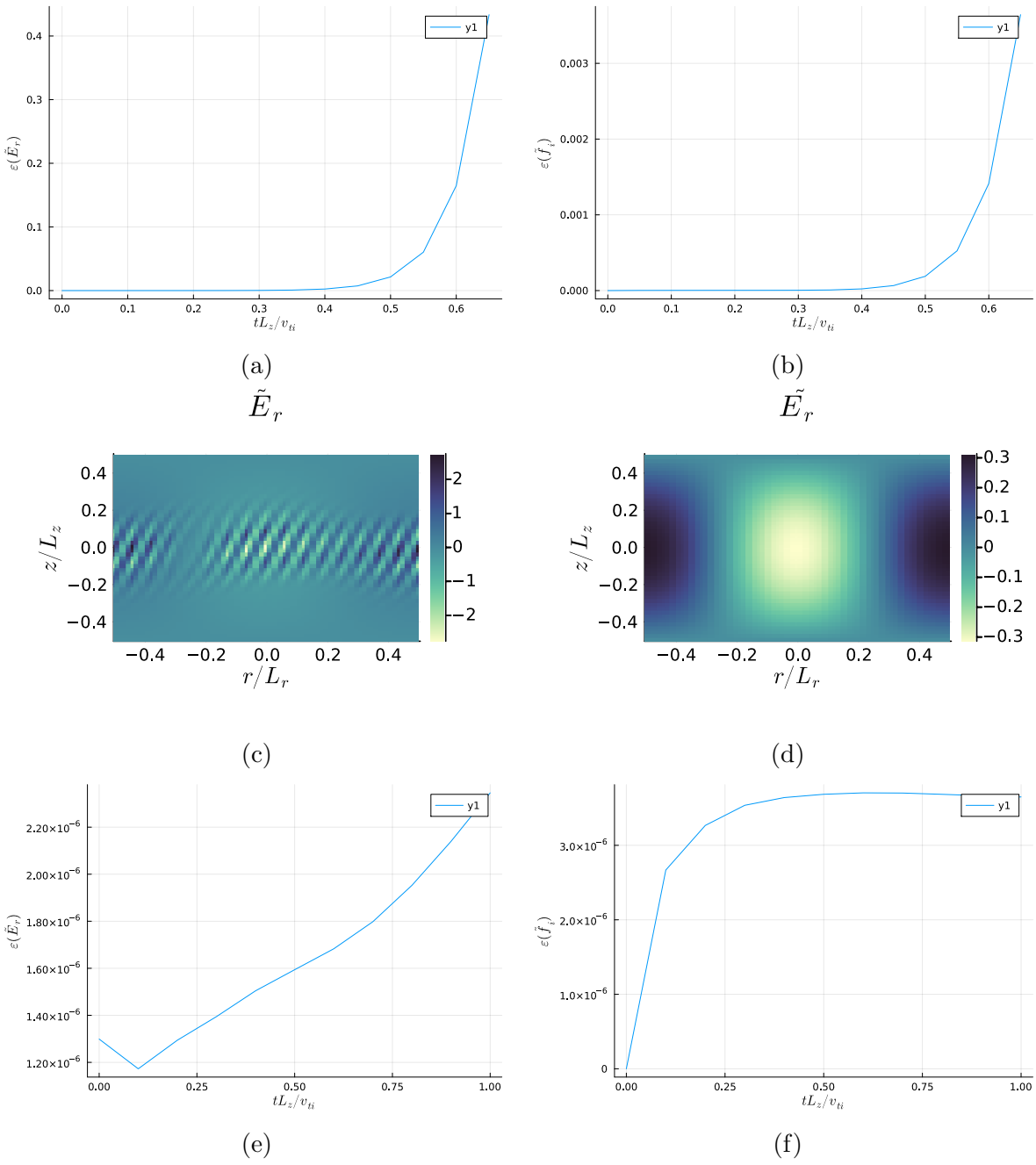

Figure 9: Plots of $\epsilon(\widetilde{f}_i)$, $\epsilon(\widetilde{E}_r)$, and $\widetilde{E}_r$ at $\tilde{t} = 0.65$ for the manufactured solutions test described in section 7 using (14). Note the exponential growth in the errors (plots (a) & (b)) suggestive of an instability, and (c) the wave-like structure forming in $\widetilde{E}_r$. When radial numerical diffusion is imposed with $\nu_r = 0.01$ (d), the wave is stabilised and the simulation can be extended to $\tilde{t} = 1.0$, with minimal errors ((e) & (f)).

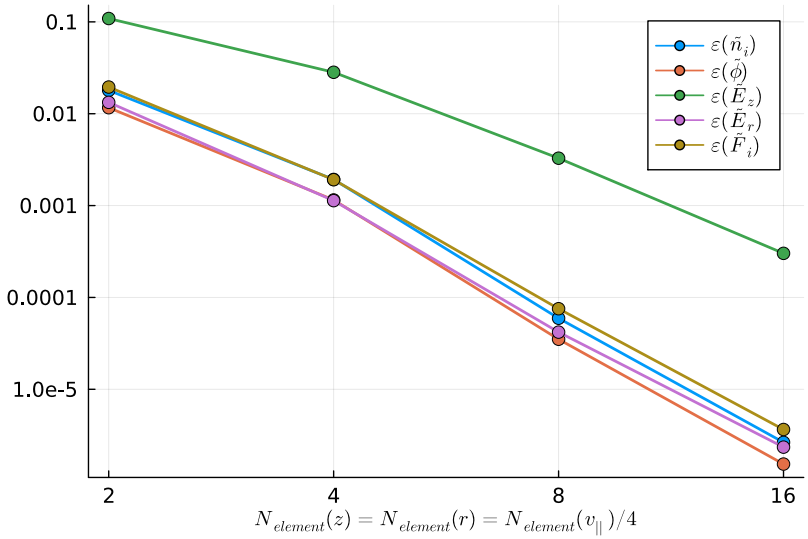

Figure 10: The MMS test with $\alpha = 0$, $p = 4$, $\rho_* = b_z = \widetilde{T}_e = \widetilde{N}_e = 1.0$, with $N_{grid} = 5$ and $N_{element}(\tilde{z})N_{element}(\tilde{r}) = N_{element}(\tilde{v}_{||})/4$. Numerical diffusion in the radial direction is applied, with $\nu_r = 0.01$, and $\nu_v = 0$. Performance comparable to that shown in figure 5 is obtained at $N_{element}(\tilde{z}) = 16$.

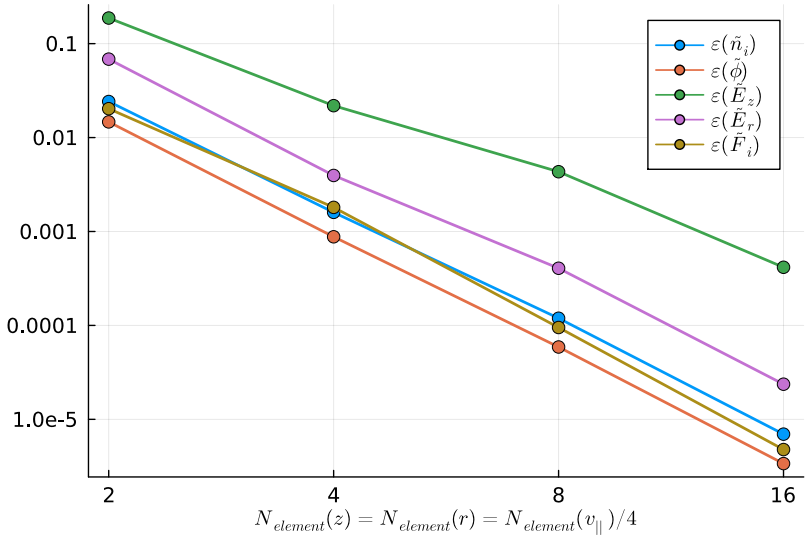

Figure 11: The MMS test with $\alpha = 1$, $p = 4$, $\rho_* = b_z = \widetilde{T}_e = \widetilde{N}_e = 1.0$, with $N_{grid} = 5$ and $N_{element}(\tilde{z})N_{element}(\tilde{r}) = N_{element}(\tilde{v}_{||})/4$. Performance is demonstrated that is comparable to that shown in figure 10.

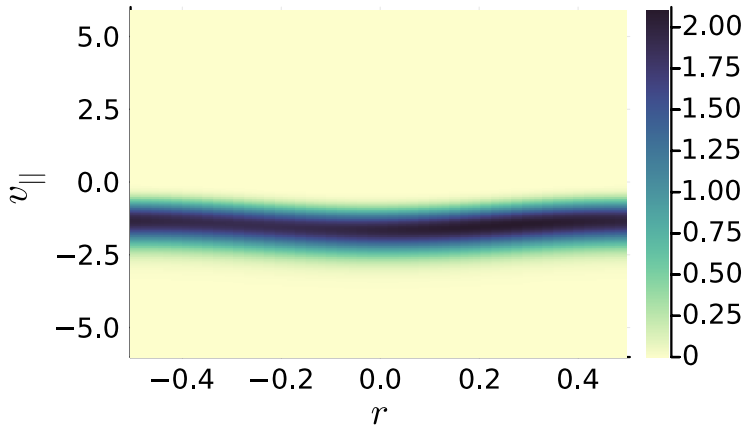

Figure 12: The ion distribution function $\widetilde{F}_i$ as a function of $(\tilde{v}_\parallel, \tilde{r})$ at the wall boundary $\tilde{z}/\tilde{L}_z = -1/2$. Compare to figure 8.

9. Convergence of physical solutions sourced by a constant ionisation rate: a cautionary tale

So far in this report, we have considered manufactured solutions where the distribution function is carefully chosen to satisfy the boundary conditions and source an electric field that does not diverge anywhere. However, in sheath problems it is typical for the electric field to diverge near the wall [6].

In this section, we examine simulations where the source is a constant, and uniform fuelling of ions through electron-neutral ionisation collisions. We take the source function to be

$$S_i = 2\exp[-4\tilde{v}_\parallel^2]. \tag{22}$$

We consider a 1D simulation where (14) is the initial condition (with $\alpha = 0$) and $p = 4$, $\rho_* = b_z = \widetilde{T}_e = \widetilde{N}_e = 1.0$, $N_{grid}(\tilde{r}) = N_{element}(\tilde{r}) = 1$, $N_{grid} = 5$ for the $\tilde{z}$ and $\tilde{v}_\parallel$ dimensions, and take $N_{element}(\tilde{z}) = N_{element}(\tilde{v}_\parallel)/4$. We take $\nu_r = 0$ and $\nu_v = 0.01$. We run for $1250N_{element}(\tilde{z})$ steps with $\Delta\tilde{t} = 0.016/N_{element}(\tilde{z})$. The total normalised time of $\tilde{t} = 20$ was found to be adequate to reach a steady-state solution. In figure 13, we show the result of scanning in $N_{element}(\tilde{z}) = N_{element}(\tilde{v}_\parallel)/4$. Figure 13a shows that $\widetilde{\phi}$ converges in the domain. The slowest convergence is observed at the wall boundaries: figure 13b indicates that $\widetilde{\phi}$ will converge with sufficient $\tilde{z}$ resolution. However, figure 13c $\widetilde{E}_z$ is diverging near the wall boundaries, although good convergence is observed in most of the domain. Figure 13d shows that $\widetilde{E}_z$ will become infinite at the wall as $N_{element}(\tilde{z}) \to \infty$. The fact that $\widetilde{\phi}$ does appear to converge indicates that the residual errors in the numerical approximation of the solution are reducing, and so the numerical solution can plausibly represent a physical solution where $\widetilde{\phi} \propto \left(1/2 \mp \tilde{z}/\tilde{L}_z\right)^q$

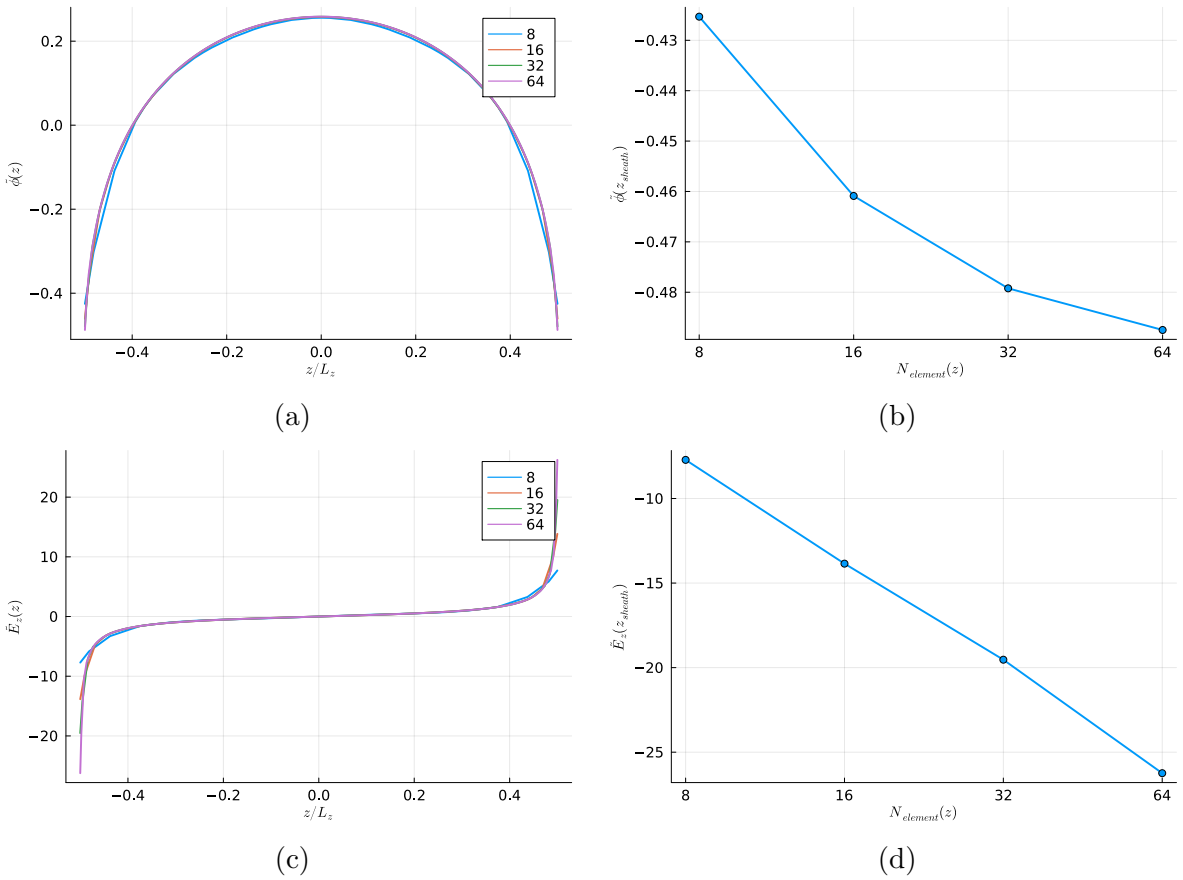

Figure 13: Plots showing the behaviour of the electrostatic potential $\widetilde{\phi}$ and the electric field $\widetilde{E}_z$ in 1D simulations where the source of ions is given by equation (22) and the initial condition is given by (14) with $\tilde{r} = 0$, $\alpha = 0$ $p = 4$, and $\rho_* = b_z = \widetilde{T}_e = \widetilde{N}_e = 1.0$. We take $\nu_r = 0$ and $\nu_v = 0.01$. We take $N_{grid} = 5$ for both the $\tilde{z}$ and $\tilde{v}_\parallel$ dimensions, with $N_{element}(\tilde{z}) = N_{element}(\tilde{v}_\parallel)/4$, and we use $\Delta\tilde{t} = 0.016/N_{element}(\tilde{z})$ with a total normalised time of $\tilde{t} = 20$. The curves are labelled by $N_{element}(\tilde{z})$. Note that whilst $\widetilde{\phi}$ appears to be converging for increasing resolution, $\widetilde{E}_z$ is diverging at the wall boundaries.

as $\tilde{z}\tilde{L}_z \to \pm 1/2$, with q real and satisfying $1 > q > 0$. The fact that $\widetilde{E}_z$ diverges in these solutions should be taken into account when making benchmarks or comparisons.

10. Discussion

In this report we have explored in detail the convergence of the spectral-element numerical implementation of the drift-kinetic 'moment kinetics' model. We have focused on the difficulties in solving the ion drift kinetic equation in the standard drift kinetic representation in 1D-1V $(\tilde{z}, \tilde{v}_\parallel)$ and 2D-1V $(\tilde{z}, \tilde{r}, \tilde{v}_\parallel)$ cases with wall boundary conditions. We have found that the most robust convergence in our manufactured solutions test can be achieved using low-order elements and high $\tilde{v}_\parallel$ resolution. We have demonstrated that the ion drift kinetic 2D1V model shows only small residual errors when a radial electric

field is included in the model, provided that adequate radial numerical dissipation is imposed to stabilise a wave-like instability. Increasing the size of the radial variation in the manufactured solutions requires a greater level of radial numerical dissipation for a successful test. This is consistent with the wave-like instability having a physical drive in the imposed manufactured solution. In addition to the manufactured solution tests, we have also shown the result of evolving the ion distribution function to steady state using a constant, uniform ionisation source. These simulations require the use of parallel velocity numerical dissipation to avoid oscillations in the profiles as a function of $\tilde{z}$, perhaps due to phase mixing or a bump-on-tail instability.

Future work will involve exploring the addition of radial inhomogeneity, vertical inhomogeneity, and a hierarchy of ion-ion collision operators. The ion-ion collision operator is crucial for providing a physical justification for the numerical diffusion imposed in the simulations described here. Radial diffusion naturally arises from ion-ion collisions interupting Larmor and radial magnetic drift orbits, whereas parallel velocity diffusion arises directly from pitch angle scattering. As our simulations here have no clear reference length scale, it is difficult to estimate whether or not the numerical diffusion that we have imposed this consistent with the physical rate of collisions in a realistic device – realistic geometry and more accurate collision models will address this issue.

Appendix A. Supporting documentation for the manufactured solutions tests

The simulations used to create the data presented in this report were generated by the branch `https://github.com/mabarnes/moment_kinetics/compare/radial-vperp-standard-DKE-Julia-1.7.2-mpi`, with the latest commit at the time of writing being `15d4b3a`.

In this appendix we give URL links to the input files used to generate the simulation data. To run a simulation use the following command

```
$ julia -O3 --project run_moment_kinetics.jl input.toml
```

To post process the simulation data and to generate the plots in this report run the following commands (after selecting the appropriate test options):

```
$ julia -O3 --project run_MMS_test.jl
```

```
$ julia -O3 --project run_evolve_convergence_test.jl
```

In supplementary data (`data/input_file_data`) we include input files simulations presented here and a script for plotting figures 6 and 7 (`data/scripts/run_derivatives_test.jl`). The simulation inputs used to generate figure 2 were

```
1D-wall_MMS_nel_r_1_z_2_vpa_2_vperp_1
1D-wall_MMS_nel_r_1_z_4_vpa_4_vperp_1
```

`1D-wall_MMS_nel_r_1_z_8_vpa_8_vperp_1`
`1D-wall_MMS_nel_r_1_z_16_vpa_16_vperp_1`.

The simulation inputs used to generate figure 3 were

`1D-wall_MMSEr_nel_r_1_z_2_vpa_2_vperp_1`
`1D-wall_MMSEr_nel_r_1_z_4_vpa_4_vperp_1`
`1D-wall_MMSEr_nel_r_1_z_8_vpa_8_vperp_1`
`1D-wall_MMSEr_nel_r_1_z_16_vpa_16_vperp_1`.

The simulation inputs used to generate figure 4 were

`1D-wall_MMSEr_ngrid_5_nel_r_1_z_8_vpa_8_vperp_1`
`1D-wall_MMSEr_ngrid_5_nel_r_1_z_16_vpa_16_vperp_1`
`1D-wall_MMSEr_ngrid_5_nel_r_1_z_32_vpa_32_vperp_1`
`1D-wall_MMSEr_ngrid_5_nel_r_1_z_64_vpa_64_vperp_1`.

The simulation inputs used to generate figure 5 were

`1D-wall_MMSEr_ngrid_5_nel_r_1_z_8_vpa_32_vperp_1`
`1D-wall_MMSEr_ngrid_5_nel_r_1_z_16_vpa_64_vperp_1`
`1D-wall_MMSEr_ngrid_5_nel_r_1_z_32_vpa_128_vperp_1`
`1D-wall_MMSEr_ngrid_5_nel_r_1_z_64_vpa_256_vperp_1`.

The simulation inputs used to generate figure 9 were

`2D-wall_MMS_ngrid_5_nel_r_16_z_16_vpa_64_vperp_1`
`2D-wall_MMS_ngrid_5_nel_r_16_z_16_vpa_64_vperp_1_diss`.

The simulation inputs used to generate figure 10 were

`2D-wall_MMS_ngrid_5_nel_r_2_z_2_vpa_8_vperp_1_diss`
`2D-wall_MMS_ngrid_5_nel_r_4_z_4_vpa_16_vperp_1_diss`
`2D-wall_MMS_ngrid_5_nel_r_8_z_8_vpa_32_vperp_1_diss`
`2D-wall_MMS_ngrid_5_nel_r_16_z_16_vpa_64_vperp_1_diss`.

The simulation inputs used to generate figure 11 were

`2D-wall_MMSEr_ngrid_5_nel_r_2_z_2_vpa_8_vperp_1_diss`
`2D-wall_MMSEr_ngrid_5_nel_r_4_z_4_vpa_16_vperp_1_diss`
`2D-wall_MMSEr_ngrid_5_nel_r_8_z_8_vpa_32_vperp_1_diss`
`2D-wall_MMSEr_ngrid_5_nel_r_16_z_16_vpa_64_vperp_1_diss`.

The simulation inputs used to generate figure 12 were

`2D-wall_MMSEr_ngrid_5_nel_r_16_z_16_vpa_64_vperp_1_diss`.

The simulation inputs used to generate figure 13 were

`1D-wall_evolve_ngrid_5_nel_r_1_z_8_vpa_32_vperp_1`
`1D-wall_evolve_ngrid_5_nel_r_1_z_16_vpa_64_vperp_1`
`1D-wall_evolve_ngrid_5_nel_r_1_z_32_vpa_128_vperp_1`
`1D-wall_evolve_ngrid_5_nel_r_1_z_64_vpa_256_vperp_1`.

Appendix B. Oversatisfying the Chodura condition in the Wall BC MMS test

For a stable sheath to exist at the wall boundary of a 2D configuration where $E_r = 0$ on the wall boundary, the ion distribution function at the sheath entrance ($z = \pm L_z/2$) must satisfy the kinetic Chodura condition [6]. The Chodura condition is the requirement that

$$Z \int \frac{v_B^2 F_i(z = z_w, \mathbf{v})}{v_\parallel^2} \, d^3\mathbf{v} \leq \frac{T_e}{e} \frac{\mathrm{d}n_e}{\mathrm{d}\phi}\Big|_{\phi=\phi_w}, \tag{B.1}$$

where Z is the ion charge and $v_B = \sqrt{ZT_e/m_i}$ is the Bohm velocity. The integration range in (B.3) is taken appropriately depending on which of the $z = \pm L_z/2$ boundaries are under consideration.

We now consider the manufactured solution (14). We also assume $T_e = T_i = T_{\mathrm{ref}}$ and $Z = 1$. Note that for a Boltzmann electron response the quantity

$$\frac{T_e}{e} \frac{\mathrm{d}n_e}{\mathrm{d}\phi}\Big|_{\phi=\phi_w} = n_i(z = z_w). \tag{B.2}$$

In terms of normalised variables, the Chodura condition thus becomes the constraint

$$\frac{1}{2} \int \int \frac{\widetilde{F}_i(z = z_w)}{\tilde{v}_\parallel^2} \, \frac{2\tilde{v}_\perp}{\sqrt{\pi}} d\tilde{v}_\perp d\tilde{v}_\parallel \leq \widetilde{n}_i(z = z_w), . \tag{B.3}$$

We choose to inspect the condition at $z = L_z/2$. We must evaluate the integral

$$\frac{1}{\sqrt{\pi}} \int_0^\infty \exp\left(-\tilde{v}_\parallel^2\right) \, d\tilde{v}_\parallel = \frac{1}{2}. \tag{B.4}$$

With this, we see that

$$\frac{1}{2} \int \int \frac{\widetilde{F}_i(z = L_z/2)}{\tilde{v}_\parallel^2} \, \frac{2\tilde{v}_\perp}{\sqrt{\pi}} d\tilde{v}_\perp d\tilde{v}_\parallel = \frac{1}{4} n_+(r). \tag{B.5}$$

Comparing to the result for the ion density, equation (15), we see that the condition (B.3) is satisfied with the equality when $\alpha = 0$ and $p = 2$ – in other words, the condition is marginally satisfied.

It is interesting to try to construct a distribution function where the condition (B.3) is oversatisfied. One candidate distribution function is (14) with $\alpha = 0$ and $p = 4$. Using the integrals

$$\frac{1}{\sqrt{\pi}} \int_0^\infty \tilde{v}_\parallel^2 \exp\left(-\tilde{v}_\parallel^2\right) \, d\tilde{v}_\parallel = \frac{1}{4}, \tag{B.6}$$

and

$$\frac{1}{\sqrt{\pi}} \int_0^\infty \tilde{v}_\parallel^4 \exp\left(-\tilde{v}_\parallel^2\right) \, d\tilde{v}_\parallel = \frac{3}{8}, \tag{B.7}$$

we find the results (15) (for $p = 4$) and

$$\frac{1}{2}\int\int \frac{\widetilde{F}_i(z = L_z/2)}{\tilde{v}_\parallel^2}\ \frac{2\tilde{v}_\perp}{\sqrt{\pi}} d\tilde{v}_\perp d\tilde{v}_\parallel = \frac{1}{8} n_+(r). \tag{B.8}$$

These results allow us to see that the Chodura condition is oversatisfied, by virtue of the fact that $n_+/8 < 3n_+/8$.

We can also evaluate the particle fluxes, with the results that when $p = 4$

$$\widetilde{\Gamma}_{-L_z/2} = \frac{b_z n_-(r)}{\sqrt{\pi}}, \quad \text{and } \widetilde{\Gamma}_{L_z/2} = \frac{b_z n_+(r)}{\sqrt{\pi}}. \tag{B.9}$$

To evaluate the fluxes, we have used the integrals

$$\frac{1}{\sqrt{\pi}}\int_0^\infty \tilde{v}_\parallel \exp\left(-\tilde{v}_\parallel^2\right)\ d\tilde{v}_\parallel = \frac{1}{2\sqrt{\pi}}, \tag{B.10}$$

$$\frac{1}{\sqrt{\pi}}\int_0^\infty \tilde{v}_\parallel^3 \exp\left(-\tilde{v}_\parallel^2\right)\ d\tilde{v}_\parallel = \frac{1}{2\sqrt{\pi}}, \tag{B.11}$$

and

$$\frac{1}{\sqrt{\pi}}\int_0^\infty \tilde{v}_\parallel^5 \exp\left(-\tilde{v}_\parallel^2\right)\ d\tilde{v}_\parallel = \frac{1}{\sqrt{\pi}}. \tag{B.12}$$

[1] Parra F I, Barnes M and Hardman M R 2021 *Excalibur/Neptune Report* 2047357–TN–07–01 M1.4

[2] Parra F I, Barnes M and Hardman M R 2021 *Excalibur/Neptune Report* 2047357–TN–09–01 M1.6

[3] Barnes M 2022 *Excalibur/Neptune Report* 2047357–TN–12

[4] Gowda S, Ma Y, Cheli A, Gwozdz M, Shah V B, Edelman A and Rackauckas C 2021 *arXiv preprint arXiv:2105.03949*

[5] URL `https://symbolics.juliasymbolics.org/dev/`

[6] Geraldini A, Parra F I and Militello F 2018 *Plasma Phys. Control. Fusion* **60** 125002

[7] Abazorius M 2023 *University of Oxford* DPhil Thesis